Journal of Power Sources 196 (2011) 3073–3082

Contents lists available at ScienceDirect

Journal of Power Sources

journal homepage: www.elsevier.com/locate/jpowsour

Three-dimensional numerical analysis of mixed ionic and electronic conducting cathode reconstructed by focused ion beam scanning electron microscope

Katsuhisa Matsuzaki [a], Naoki Shikazono [b,*], Nobuhide Kasagi [a]

[a] Department of Mechanical Engineering, The University of Tokyo, Hongo 7-3-1, Bunkyo-ku, Tokyo 113-8656, Japan
[b] Institute of Industrial Science, The University of Tokyo, Komaba 4-6-1, Meguro-ku, Tokyo 153-8505, Japan

ARTICLE INFO

Article history:
Received 18 September 2010
Received in revised form
21 November 2010
Accepted 26 November 2010
Available online 2 December 2010

Keywords:
Solid oxide fuel cell
Cathode
Mixed ionic and electronic conductor
Lattice Boltzmann method
Focused ion beam scanning electron microscopy

ABSTRACT

Three-dimensional microstructure of mixed ionic and electronic conducting cathode, $La_{0.6}Sr_{0.4}Co_{0.2}Fe_{0.8}O_{3-\delta}$ (LSCF6428), is obtained by a dual-beam focused ion beam-scanning electron microscope, and its overpotential is predicted by the lattice Boltzmann method. Gaseous, ionic and electronic transport equations coupled with electrochemical reaction at the gas/solid interface in the three-dimensional microstructure are solved with an assumption of local equilibrium in the solid oxide. The gas transport is modeled by the dusty gas model. The numerical simulation is conducted under the current density conditions of 0.01, 0.05, 0.1 and 0.2 A/cm^2. Predicted cathode overpotentials agreed well with the experimental results. However, predicted overpotential was very large at O_2 = 20%, T = 973 K and i = 0.2 A/cm^2 case due to the decline of ionic conductivity at low oxygen partial pressure. Three-dimensional chemical potential and current vector distributions inside LSCF microstructure are presented. Ionic and electronic current stream lines are uniform and smooth, which indicates good ionic and electronic conductions as well as wide electrochemically active areas inside the LSCF microstructure. Present method will be an effective tool for investigating local oxygen potential field which affects local reactions, diffusions and physical properties of the MIEC cathodes.

1. Introduction

A solid oxide fuel cell (SOFC) is expected to be a promising energy conversion device in the future because of its high efficiency and fuel flexibility [1]. Cost reduction and long-term durability are the major issues for the development of SOFC system. One of the promising approaches is the reduction of operating temperature, which promotes utilization of low cost metals in the system. On the other hand, low temperature operation leads to poor performance of the cell due to the degradations of conductivities and polarization characteristics. Thus, great efforts have been paid for developing efficient and stable materials for the electrodes. Mixed ionic and electronic conductors (MIECs) such as $La_{1-x}Sr_xCoO_{3-\delta}$ (LSC) or $La_{1-x}Sr_xCo_{1-y}Fe_yO_{3-\delta}$ (LSCF) are expected to be very effective in reducing polarization losses of the electrodes [2,3]. Polarization characteristics of MIEC electrodes depend on electrochemical reaction rates at the gas/solid interface, and diffusions of ion, electron and gas species, which are strongly affected by the microstructure. Recently, direct measurements of three-dimensional SOFC electrode microstructures have been conducted by focused ion beam scanning electron microscopy (FIB-SEM) [4–7] and X-ray computed tomography (XCT) [8,9]. Through these three-dimensional measurements, important microstructural parameters such as three phase boundary (TPB) length and tortuosity factors can be obtained. For example, in Gostovic et al. [5], three-dimensional microstructure of LSCF cathode was reconstructed by FIB-SEM and the relationship between cathodic polarization and surface area or tortuosity has been investigated.

In order to discuss quantitative relationship between electrode microstructures and their polarization characteristics, numerical simulations are expected to provide useful information which cannot be obtained from experiments. Joshi et al. [10] performed a multi-component lattice Boltzmann method (LBM) simulation in a two-dimensional porous media. Asinari et al. [11] also used LBM for solving H_2 and H_2O diffusion inside the micro pores. Suzue et al. [12] conducted a three-dimensional LBM simulation which solves the species transport coupled with the electrochemical reaction in a stochastically reconstructed anode microstructure. Shikazono et al. [13] used Ni/YSZ anode microstructure reconstructed by FIB-SEM and solved transport equations and electrochemical reactions at TPB using LBM. Three-dimensional potential and current vector distributions inside actual Ni/YSZ anode are demonstrated. Shearing et al. [14] conducted volume of fluid (VOF) simulation of electrochemical reaction and diffusion inside Ni/YSZ anode obtained from FIB-SEM measurement. In the above-mentioned models, however, each of the solid phases is assumed to be either perfect electronic or

* Corresponding author. Tel.: +81 3 5452 6776; fax: +81 3 5452 6776.
E-mail address: shika@iis.u-tokyo.ac.jp (N. Shikazono).

0378-7753/$ – see front matter © 2010 Elsevier B.V. All rights reserved.
doi:10.1016/j.jpowsour.2010.11.142

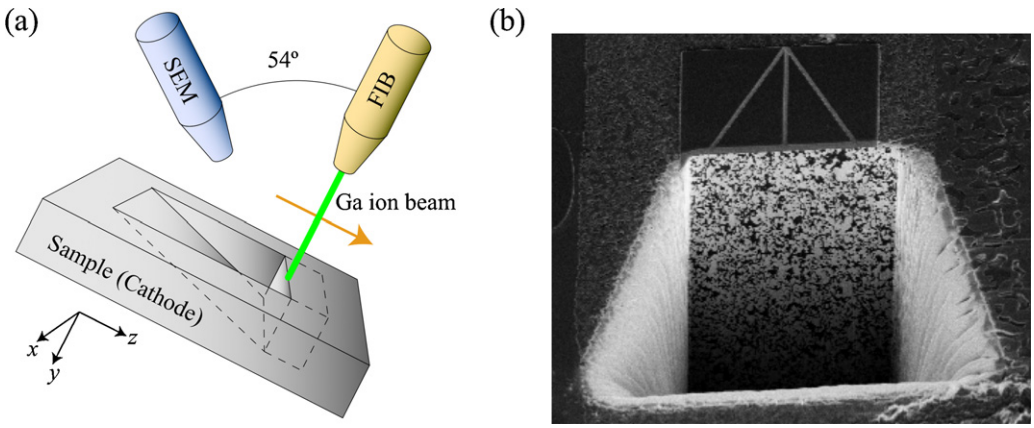

Fig. 1. (a) Schematic diagram of FIB-SEM setting and (b) reference marks milled on top surface.

ionic conductors, not MIECs. As a result, electrochemical reaction only takes place at the TPB. On the other hand, electrochemical reaction can be active at wide area of gas/solid interface in the case of MIEC electrodes, since both electrons and ions can exist in the single solid phase. In order to design and optimize MIEC electrodes, it is very effective to use numerical simulation tools which can describe species diffusions and charge transfer inside complex electrode microstructure.

In the present study, the three-dimensional microstructure of $La_{0.6}Sr_{0.4}Co_{0.2}Fe_{0.8}O_{3-\delta}$ (LSCF6428) cathode is quantified by a dual beam FIB-SEM. Marching cube method is used to quantify surface area from voxel structures. Assuming surface electron transfer to be the rate limiting step, reaction current is expressed by a Butler–Volmer like form [15]. Transport equations for electron, oxide ion and gas species coupled with charge transfer at gas/solid interface in the three-dimensional field is solved by the lattice Boltzmann method. Predicted overpotential is compared with the experimental data for validation. Finally, three-dimensional chemical potential and current vector distributions inside LSCF microstructure are presented.

2. Sample preparation and 3D microstructure reconstruction

In the present study, electrolyte supported button cell with LSCF cathode and Ni/YSZ anode is used (Japan Fine Ceramics Co., Ltd.). Press molded 8YSZ electrolyte disk was sintered at 1500 °C, followed by the GDC10 interlayer sintering at 1500 °C. NiO–8YSZ (60:40 wt%) anode and LSCF6428 cathode were sintered at 1300 and 1000 °C, respectively.

Observation and quantification of the three-dimensional microstructure of the LSCF6428 cathode are facilitated by FIB-SEM (Carl Zeiss, NVision 40) [7]. The sample was infiltrated with epoxy resin (Marumoto Struers KK) under vacuum so that the pores could be easily distinguished during SEM observation. Fig. 1 schematically shows a typical setting for the FIB-SEM measurement. In this study, an in-lens secondary electron detector was used with acceleration voltage of 1.5 kV. By automatically repeating FIB milling and SEM imaging sequence, a series of cross sectional images necessary for three-dimensional structure reconstruction is acquired. Reference marks are created on the carbon deposition layer on the sample surface to assist the alignment of SEM images, as shown in Fig. 1(b).

Separation of solid and pore phases is carried out for each SEM image. Epoxy infiltration enables easy binarization of the phases as shown in Fig. 2(a). As the LBM simulation requires cubic meshing, the resolution of each cross sectional image was coarsened from 13.96 nm/pixel to 59.18 nm/pixel which is the FIB milling pitch as shown in Fig. 2(b). The phase which has larger area portion was chosen as the representative phase for the coarser mesh. Fig. 3 shows the reconstructed three-dimensional microstructure. Original SEM

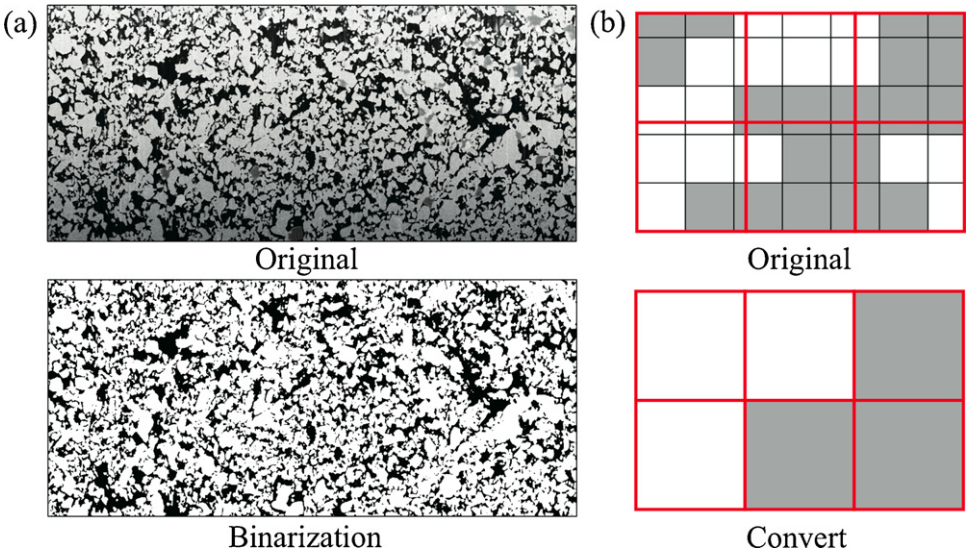

Fig. 2. (a) Phase separation and (b) mesh alignment for voxel reconstruction (white: LSCF, black: pore).

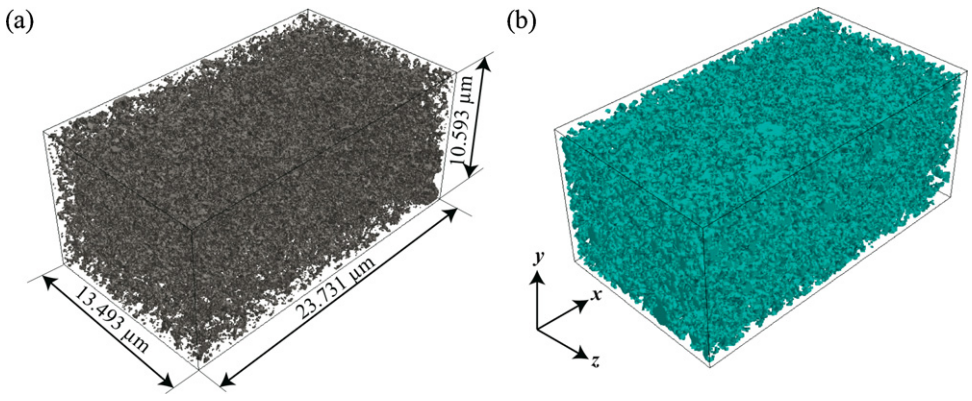

Fig. 3. Reconstructed 3D cathode microstructure: (a) pore phase and (b) LSCF phase.

images correspond to *x*–*y* cross sections, and FIB milling is carried out in *z*-direction.

If gas/solid interface is simply defined by the voxel surface, surface area will be considerably overestimated. In the present study, marching cube method [16] is used to calculate the surface area. Marching cube method considers 21 patterns to calculate interface area from the phase information of neighboring 8 voxels as shown in Fig. 4. However, it is reported that marching cube method still overestimates surface area by approximately 8% in the case of sphere [17]. Table 1 shows the surface area of the reconstructed microstructure calculated by the marching cube method and stereology [18]. Surface area is calculated for divided regions shown in Fig. 5 to check variation between the samples. Surface areas from *x*-divided and *y*-divided samples show very small variations, while quite large variation is found between *z*-divided samples. It is considered that the error caused from the image alignment procedure in the FIB milling direction (*z*-direction) is the possible reason for the variation between *z*-divided samples. Marching cube method gives fairly good agreement with stereology at the same resolution of 59.18 nm/pixel. However, stereology results show dependency on resolution, and it should be considered that the present marching cube results also contain grid resolution dependence.

Table 1
Surface areas calculated by marching cube method and stereology for different regions.

Structure	Volume [μm^3]	Surface area density [$\mu m^2/\mu m^3$]
Original	$23.731 \times 10.593 \times 13.493$	6.765
x-axis divided	$5.918 \times 10.593 \times 13.493$	6.641 6.813 6.866 6.667
y-axis divided	$23.731 \times 5.267 \times 13.493$	6.666 6.831
z-axis divided	$23.731 \times 10.593 \times 6.747$	7.145 6.358
Stereology [18]	(Resolution: 13.96 nm/px) (Resolution: 59.18 nm/px)	7.734 (σ: 0.859) 6.035 (σ: 0.536)

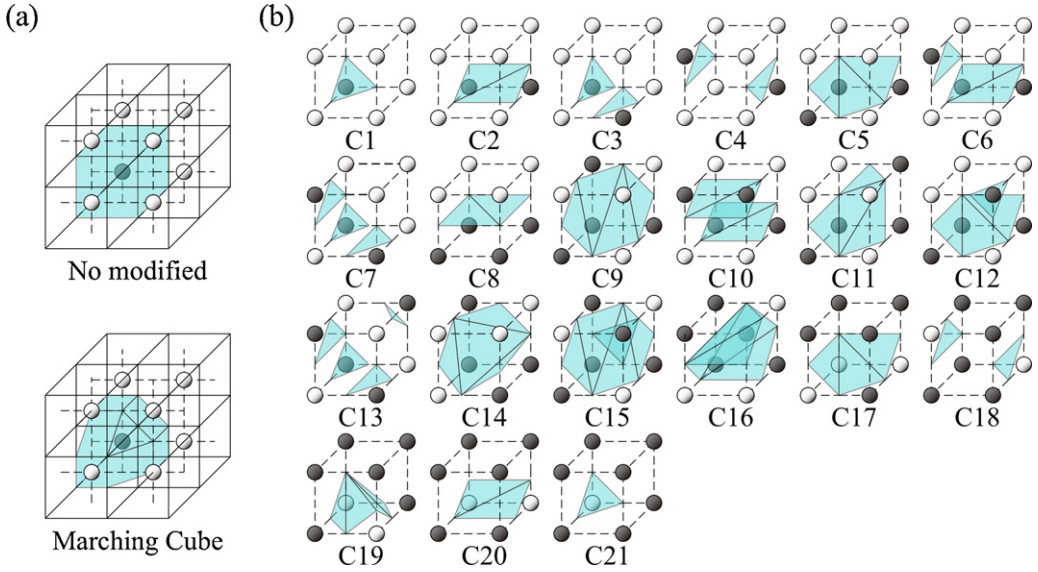

Fig. 4. Marching cube method for surface area calculation. Black and white spheres represent phase information of each voxel and estimated interface is colored in blue. (a) Example with one black phase and seven white phases in neighboring eight voxels. (b) 21 interface patterns used in marching cube calculation. (For interpretation of the references to color in this figure legend, the reader is referred to the web version of the article.)

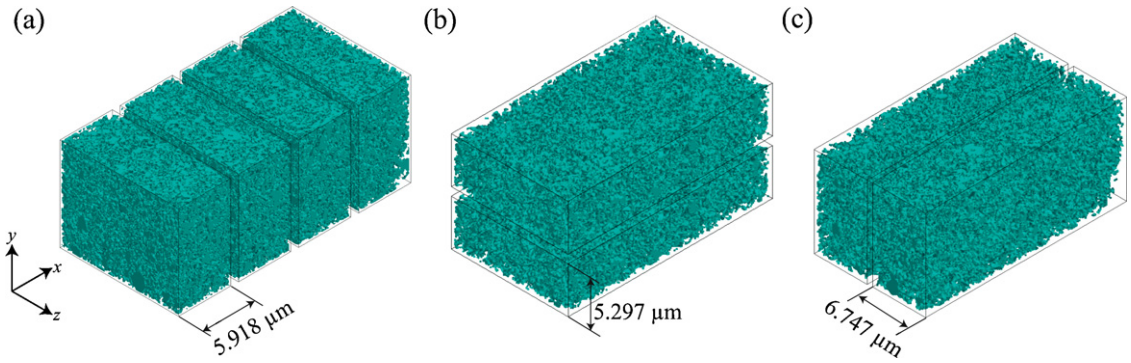

Fig. 5. Divided structures: (a) *x*-axis divided, (b) *y*-axis divided, and (c) *z*-axis divided.

Table 2
Gas diffusion parameters used in Eqs. (4)–(7).

Substance	M [kg/mol]	ζ [Å]	ε/k [K]
O_2	31.9988×10^{-3}	3.54	88.0
N_2	28.0314×10^{-3}	3.68	91.5

3. Numerical analysis by the lattice Boltzmann method

3.1. Diffusion equations

In the pore phase, diffusions of oxygen and nitrogen are solved based on the dusty gas model (DGM) [19]. Convection is neglected and constant total pressure is assumed in the present study for the first order approximation.

$$\frac{\mathbf{N}_i}{D_{i,k}} + \sum_{j \neq i} \frac{y_j \mathbf{N}_i - y_i \mathbf{N}_j}{D_{i,j}} = -\nabla C_i, \tag{1}$$

where y_i is the molar fraction and $\mathbf{N}_i$ is the molar flux. Subscripts i and j present gas species, such as oxygen and nitrogen. For constant total pressure, Graham's law holds:

$$\sum_i \mathbf{N}_i \sqrt{M_i} = 0. \tag{2}$$

Therefore, the diffusion equation of oxygen can be expressed as:

$$\nabla \left(\left[\frac{1 - \alpha y_{O_2}}{D_{O_2,N_2}} + \frac{1}{D_{O_2,k}} \right]^{-1} \nabla C_{O_2} \right) = -\frac{1}{4F} i_{reac}, \tag{3}$$

$$\alpha = 1 - \sqrt{\frac{M_{O_2}}{M_{N_2}}}. \tag{4}$$

In Eq. (3), D_{O_2,N_2} and $D_{O_2,k}$ represent binary and Knudsen diffusion coefficients, respectively:

$$D_{O_2,N_2} = 0.018833 \sqrt{\frac{1}{M_{O_2}} + \frac{1}{M_{N_2}}} \frac{T^{3/2}}{P \Omega_D \zeta_{O_2,N_2}^2}, \tag{5}$$

$$D_{O_2,k} = \frac{2}{3} \sqrt{\frac{8RT}{\pi M_{O_2}}} r. \tag{6}$$

where Ω_D is the collision integral given as:

$$\Omega_D = 1.1336 \left(\frac{Tk}{\varepsilon} \right)^{-0.1814}. \tag{7}$$

When calculating binary diffusion coefficient, an intermolecular force constants ζ is taken as an arithmetic mean of ζ_{O_2} and ζ_{N_2}. Geometric mean of ε_{O_2} and ε_{N_2} is used for ε. The gas parameters are shown in Table 2. The mean pore radius is calculated by the maximum sphere inscription method (MSI) [20]. In MSI, a sphere with radius $r = h/2$ is initially inserted in each pore voxel of size h. Then, the sphere radius is increased until the sphere contains at least one solid phase voxel inside. This radius is assigned as pore radius for every voxels that are included in the sphere. Local pore radius is given by taking the maximum of the assigned radii at each voxel. In the present LSCF sample, the mean pore radius of $r = 89$ nm is obtained by taking the average of local radii.

Electronic and ionic transport equations are solved in the solid MIEC phase:

$$\nabla \left(\frac{\sigma_{e^-}}{F} \nabla \tilde{\mu}_{e^-} \right) = -i_{reac}, \tag{8}$$

$$\nabla \left(\frac{\sigma_{O^{2-}}}{2F} \nabla \tilde{\mu}_{O^{2-}} \right) = i_{reac}, \tag{9}$$

where $\tilde{\mu}_{e^-}$, $\tilde{\mu}_{O^{2-}}$, σ_{e^-} and $\sigma_{O^{2-}}$ are electrochemical potentials and conductivities of electron and oxide ion, respectively. In a mixed conductor, σ_{e^-} and $\sigma_{O^{2-}}$ depend on local oxygen potential and temperature. In the present study, σ_{e^-} and chemical diffusion coefficient of oxide ion $\tilde{D}$ are fitted from the experimental data of Bouwmeester et al. [21].

$$\log_{10} \sigma_{e^-} = -0.0237 (\log_{10} p_{O_2})^2 + 0.0034 \cdot \log_{10} p_{O_2} + 4.8126 \quad (1073.15\,K), \tag{10}$$

$$\log_{10} \sigma_{e^-} = -0.0222 (\log_{10} p_{O_2})^2 - 0.0169 \cdot \log_{10} p_{O_2} + 4.8056 \quad (1023.15\,K), \tag{11}$$

$$\log_{10} \sigma_{e^-} = -0.0095 (\log_{10} p_{O_2})^2 - 0.0011 \cdot \log_{10} p_{O_2} + 4.8152 \quad (973.15\,K), \tag{12}$$

$$\log_{10} \sigma_{e^-} = -0.008 (\log_{10} p_{O_2})^2 - 0.0024 \cdot \log_{10} p_{O_2} + 4.8447 \quad (923.15\,K), \tag{13}$$

$$\log_{10} \tilde{D} = -0.1765 (\log_{10} p_{O_2})^2 - 0.2724 \cdot \log_{10} p_{O_2} - 9.2256 \quad (1073.15\,K), \tag{14}$$

$$\log_{10} \tilde{D} = -0.1884 (\log_{10} p_{O_2})^2 - 0.3243 \cdot \log_{10} p_{O_2} - 9.4969 \quad (1023.15\,K), \tag{15}$$

$$\log_{10} \tilde{D} = -0.1882 (\log_{10} p_{O_2})^2 - 0.2491 \cdot \log_{10} p_{O_2} - 9.7676 \quad (973.15\,K), \tag{16}$$

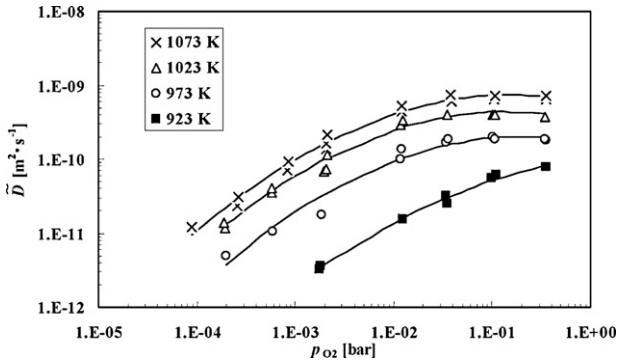

Fig. 6. Chemical diffusion coefficient of LSCF6428 from Bouwmeester et al. [21]. Solid lines represent fitting curves, Eqs. (14)–(17).

$$\log_{10}\tilde{D} = -0.1252(\log_{10} p_{O_2})^2 - 0.2051 \cdot \log_{10} p_{O_2} - 9.9554 \quad (923.15\,\mathrm{K}). \tag{17}$$

Assuming prevailing electronic conductivity of the perovskites, chemical diffusion coefficient $\tilde{D}$ is related to the ionic conductivity $\sigma_{O^{2-}}$ as:

$$\tilde{D} = \frac{1}{4F^2}\frac{\sigma_{O^{2-}}\sigma_{e^-}}{\sigma_{O^{2-}}+\sigma_{e^-}}\frac{\partial \mu_O}{\partial c_O} \approx -\frac{RTV_m}{8F^2}\sigma_{O^{2-}}\frac{\partial \ln p_{O_2}}{\partial \delta}, \tag{18}$$

where c_O is the concentration of oxygen in the perovskite, and $V_m = 35.5 \times 10^{-6}\,m^3/mol$ is the molar volume of LSCF. Oxygen non-stoichiometry δ and oxygen partial pressure p_{O_2} is again fitted from the data of Bouwmeester et al. [21]:

$$\frac{\partial \delta}{\partial \ln p_{O_2}} = -3.36260 \times 10^{-5} \cdot T + 2.59403 \times 10^{-2}. \tag{19}$$

Fig. 6 shows the chemical diffusion coefficients of Bouwmeester et al. [21]. Solid lines in Fig. 6 represent the fitting curves using Eqs. (14)–(17). As described in Eq. (19), almost linear relationship is found between δ and $\log p_{O_2}$, which means that $\tilde{D}$ and $\sigma_{O^{2-}}$ show nearly the same trend against p_{O_2}. Profound decline in chemical diffusion coefficient below p_{O_2} of 10^{-2} bar shown in Fig. 6 is considered to be due to the ordering of oxygen vacancies, which is induced by the increased vacancy concentration and the enhanced interactions between the vacancies [21].

Local oxygen partial pressure in the solid phase is calculated assuming local equilibrium:

$$\mu_O = \tilde{\mu}_{O^{2-}} - 2\tilde{\mu}_{e^-}, \tag{20}$$

$$\mu_O = \frac{1}{2}RT \log p_{O_2}. \tag{21}$$

3.2. Electrochemical reaction at gas/solid interface

In MIEC electrodes, charge transfer at the gas/solid interface becomes dominant. According to Fleig et al. [15,22], electron transfer to an adsorbed O_{ad} atom at the gas/solid interface is assumed to be the rate limiting step in the LSCF cathode reaction:

$$O_{ad} + e^- \rightarrow O^-_{ad}. \tag{22}$$

If overpotential is applied to the electrode, gas/solid interface potential step χ deviates from its equilibrium value χ^{eq} as:

$$\Delta\chi = \chi - \chi^{eq} = \varphi_{ode} - \varphi_{ad} - (\varphi^{eq}_{ode} - \varphi^{eq}_{ad}). \tag{23}$$

Assuming that subsequent elementary steps are at equilibrium and ion conduction in the electrolyte is fast, surface potential step $\Delta\chi$ and electrode activation overpotential η_{act} can be related as:

$$2\eta_{act} = \Delta\chi + \frac{RT}{F}\ln\left(\frac{\theta_{O^-_{ad}}}{1-\theta_{O^-_{ad}}}\frac{1-\theta^{eq}_{O^-_{ad}}}{\theta^{eq}_{O^-_{ad}}}\right), \tag{24}$$

where, $\theta_{O^-_{ad}}$ denotes surface coverage of O^-_{ad}. If the surface has high number of surface sites and surface coverage is moderate, i.e. $\theta_{O^-_{ad}} \approx \theta^{eq}_{O^-_{ad}}$, the second term in the R.H.S of Eq. (24) can be neglected. Then, $2\eta_{act} = \Delta\chi$ holds, and Butler–Volmer like equation with an additional factor of two in the exponents can be used for the reaction current at the gas/solid interface [15].

$$i_{reac,2PB} = i_0 A_{2PB}\left\{\exp\left(\frac{2\alpha F}{RT}\eta_{act}\right) - \exp\left(-\frac{2(1-\alpha)F}{RT}\eta_{act}\right)\right\}. \tag{25}$$

According to the experimental data of dense LSCF cathode [22], Tafel lines with slopes of $1.2F/RT$ and $1.0F/RT$ in anodic and cathodic regimes are observed. In the present study, following equation is used for the reaction current at the gas/solid interface as a function of activation overpotential η_{act}:

$$i_{reac,2PB} = i_0 A_{2PB}\left\{\exp\left(\frac{1.2F}{RT}\eta_{act}\right) - \exp\left(-\frac{1.0F}{RT}\eta_{act}\right)\right\}. \tag{26}$$

Oxygen partial pressure dependence and activation energy of the lineal exchange current i_0 is fitted from the experimental data

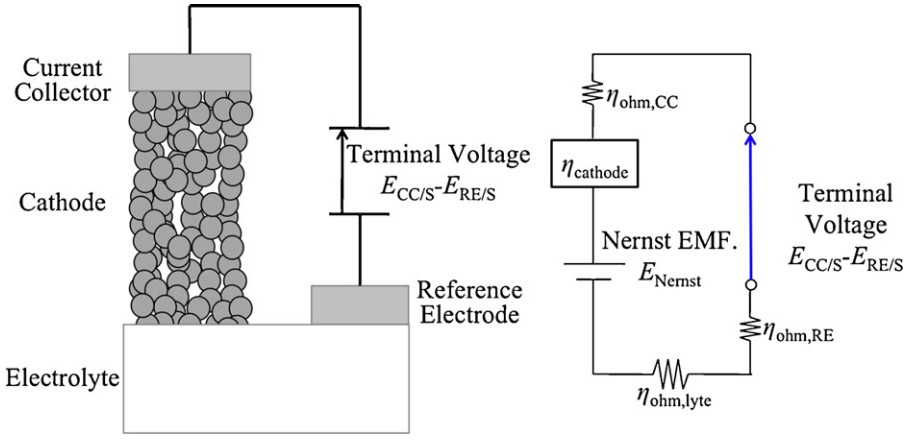

Fig. 7. Total cathode overpotential.

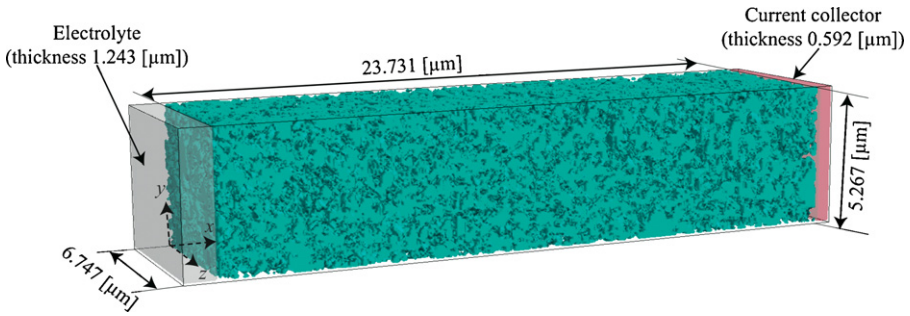

Fig. 8. Computational domain (red: current collector; gray: electrolyte; green: LSCF). (For interpretation of the references to color in this figure legend, the reader is referred to the web version of the article.)

of Esquirol et al. [23].

$$i_0 = 1.47 \times 10^6 \cdot p_{O_2}^{0.2} \cdot \exp\left(-\frac{85859}{RT}\right). \tag{27}$$

The coefficient 1.47×10^6 in Eq. (27) is chosen so that the prediction fits most to the experimental data shown in Section 4.

Local activation overpotential η_{act} at gas/solid interface is defined as:

$$\eta_{act} = -\frac{1}{2F}\left(2\tilde{\mu}_{e^-,MIEC} - \tilde{\mu}_{O^{2-},MIEC} + \frac{1}{2}RT\log p_{O_2,gas}\right). \tag{28}$$

The total cathode overpotential $\eta_{cathode}$ is obtained by subtracting ohmic losses of current collector (CC), electrolyte and reference electrode (RE) from the total overpotential, defined as the difference between EMF and terminal voltage as shown in Fig. 7.

$$\begin{aligned}\eta_{cathode} &= E_{Nernst} - (E_{CC/S} - E_{RE/S}) - \eta_{ohm,CC} - \eta_{ohm,lyte} - \eta_{ohm,RE}\\ &= \frac{RT}{4F}\log\left(\frac{p_{O_2,CC}}{p_{O_2,RE}}\right) - \frac{1}{F}(\tilde{\mu}_{e^-,RE/S} - \tilde{\mu}_{e^-,CC/S})\\ &\quad -\frac{1}{F}(\tilde{\mu}_{e^-,CC/S} - \tilde{\mu}_{e^-,cathode/CC}) - \frac{1}{2F}(\tilde{\mu}_{O^{2-},cathode/lyte} - \tilde{\mu}_{O^{2-},lyte/RE})\\ &\quad -\frac{1}{F}(\tilde{\mu}_{e^-,lyte/RE} - \tilde{\mu}_{e^-,RE/S})\\ &= \frac{RT}{4F}\log\left(\frac{p_{O_2,CC}}{p_{O_2,RE}}\right) - \frac{1}{2F}(\tilde{\mu}_{O^{2-},cathode/lyte} - 2\tilde{\mu}_{e^-,cathode/CC} - \mu_{O,lyte/RE})\\ &= -\frac{1}{2F}\left(\tilde{\mu}_{O^{2-},cathode/lyte} - 2\tilde{\mu}_{e^-,cathode/CC} - \frac{1}{2}RT\log p_{O_2,CC}\right).\end{aligned} \tag{29}$$

Table 3
Numerical conditions for the present work.

Properties	Value
Operating temperature, T [K]	973.15 1023.15 1073.15
Total pressure, P [Pa]	1.013×10^5
Gas composition (O_2:N_2) [mol%]	100:0 50:50 20:80
Current density, i [A/cm^2]	0.01 0.05 0.1 0.2

3.3. Numerical scheme

The lattice Boltzmann method (LBM) is used to solve Eqs. (3), (8) and (9). For three-dimensional LBM simulation, D3Q15 (i = 1–15) or D3Q19 (i = 1–19) models are commonly used. However, in the case of simple diffusion simulation, it has been shown that D3Q6 (i = 1–6) model can be used with a slight loss of accuracy [24]. Thus, the D3Q6 model is used in this study.

The lattice Boltzmann equation with the LBGK model in the collision term is written as follows:

$$f_i(\mathbf{x} + \mathbf{c}_i\Delta t, t + \Delta t) = f_i(\mathbf{x}, t) - \frac{1}{t^*(\mathbf{x}, t)}[f_i(\mathbf{x}, t) - f_i^{eq}(\mathbf{x}, t)] + w_i\Delta t. \tag{30}$$

In Eq. (30), f_i represents the density distribution function of gas, electron or ion with a velocity $\mathbf{c}_i$ in the i-th direction, and f_i^{eq} is the Maxwellian local equilibrium distribution,

$$f_i^{eq} = \frac{1}{6}\sum_{i=1}^{6} f_i(\mathbf{x}, t). \tag{31}$$

The relaxation time t^* is a function of diffusion coefficient D, voxel size Δx and time step Δt and it given as:

$$t^*(\mathbf{x}, t) = 0.5 + \frac{D(\mathbf{x}, t)\Delta t}{3\Delta x^2}, \tag{32}$$

In this study, diffusion coefficient of gas, electronic conductivity and ionic conductivity are spatially non-uniform, so the relaxation time is varied locally during the calculation.

For reducing computational time, the volume is halved in y and z directions. The electrolyte layer is added at x = 0 μm, and the current collector (CC) is set at x = 23.731 μm. Thicknesses of electrolyte and CC layers are 1.243 μm and 0.592 μm, respectively. The resultant computational domain is represented by 432 × 90 × 115 voxels, as shown in Fig. 8. The differences of specific surface area and volume fraction between the reduced size structure and the original structure were less than 5%.

Adiabatic boundary condition is applied at the boundaries of y = 0, 5.267 μm and z = 0, 6.747 μm. Constant gas composition (Dirichlet boundary) is given at the current collector surface. Constant electronic and ionic current flux conditions (Neumann boundary) are imposed on the current collector and electrolyte boundaries, respectively. A zero-flux boundary is imposed on the solid surface in the porous media by applying the halfway

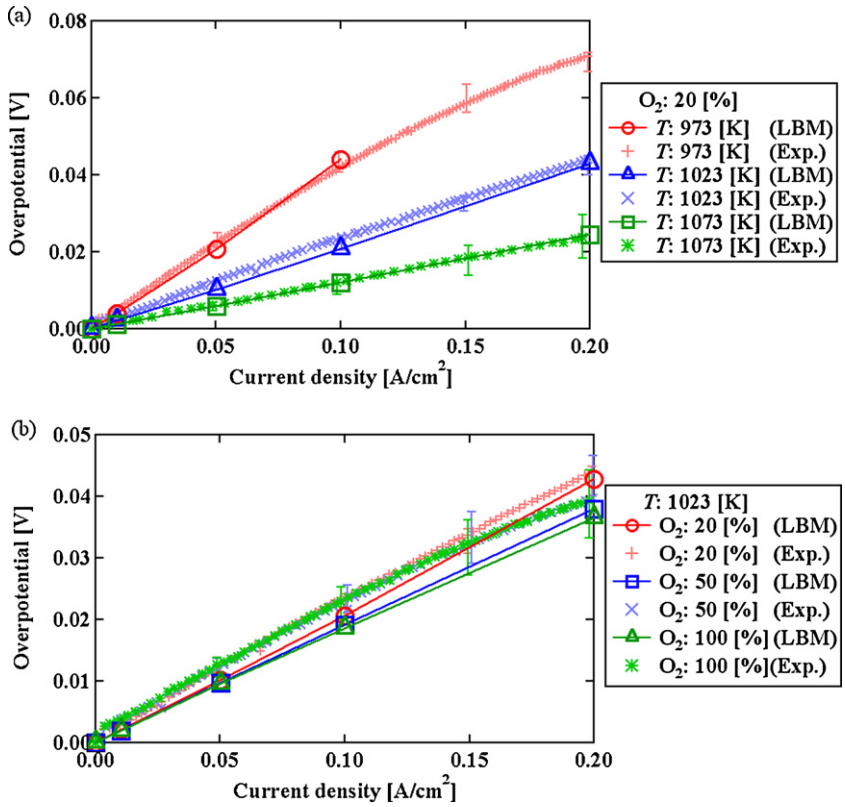

Fig. 9. Comparison of cathode overpotential. (a) Temperature dependence at O_2 = 20%, and (b) oxygen potential dependence at T = 1023 K.

bounceback scheme with a second-order accuracy. The numerical conditions are shown in Table 3.

4. Computational results

Predicted overpotential is compared with the experimental results in Fig. 9. Fig. 9(a) shows temperature dependence at O_2 = 20%, and (b) shows oxygen potential dependence at T = 1023 K. The error bars represent standard deviations of the experimental data. Prediction shows quantitative agreement with the experimental data. However, the predicted overpotential value at O_2 = 20%, T = 973 K, i = 0.2 A/cm^2 case was considerably large, approximately 0.19 V. Since this value is far beyond the vertical axis range of Fig. 9(a), the predicted point is not shown in the figure. This overprediction can be attributed to the reduction of chemical diffusion coefficient of LSCF at low oxygen partial pressures and

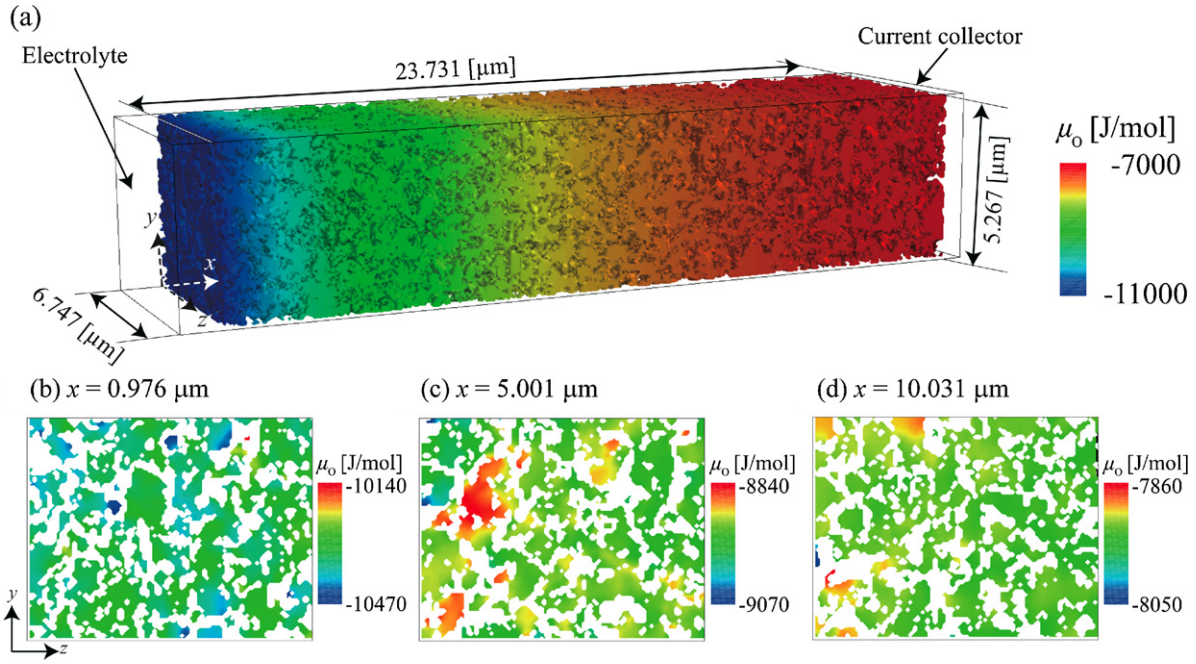

Fig. 10. Oxygen chemical potential μ_O distribution in LSCF cathode at T = 1023 K, O_2 = 20%, i = 0.1 A/cm^2.

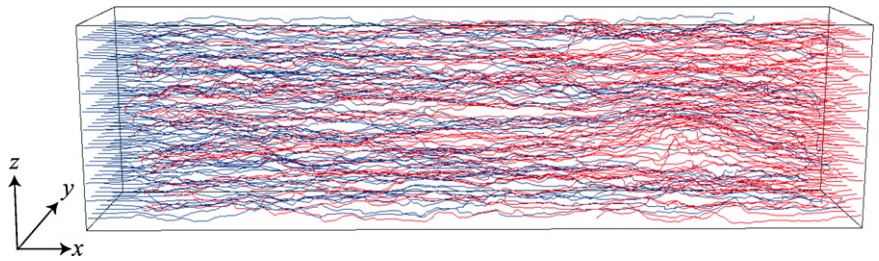

Fig. 11. Three-dimensional current stream lines in LSCF cathode (red: electronic current; blue: ionic current) at $T = 1023$ K, $O_2 = 20\%$, $i = 0.1$ A/cm^2. (For interpretation of the references to color in this figure legend, the reader is referred to the web version of the article.)

low temperatures shown in Fig. 6. It is considered that potential drop near the electrolyte side of the LSCF layer lead to degradation of ionic conductivity, which further decreased the potential. This positive feedback caused the diverged prediction of overpotential at low temperature and large current density condition.

Fig. 10 shows three-dimensional oxygen chemical potential μ_O distribution at $T = 1023$ K, $O_2 = 20\%$, $i = 0.1$ A/cm^2. Note that color scales in Fig. 10(b)–(d) for the cross sectional planes are magnified so that very small potential difference can be identified. Oxygen chemical potential is nearly uniform in the cross sectional plane, and potential gradually drops from the current collector to the electrolyte. Fig. 11 shows three-dimensional current stream lines. Electronic and ionic current stream lines are nearly straight and parallel, which indicates good ionic and electronic conductions in

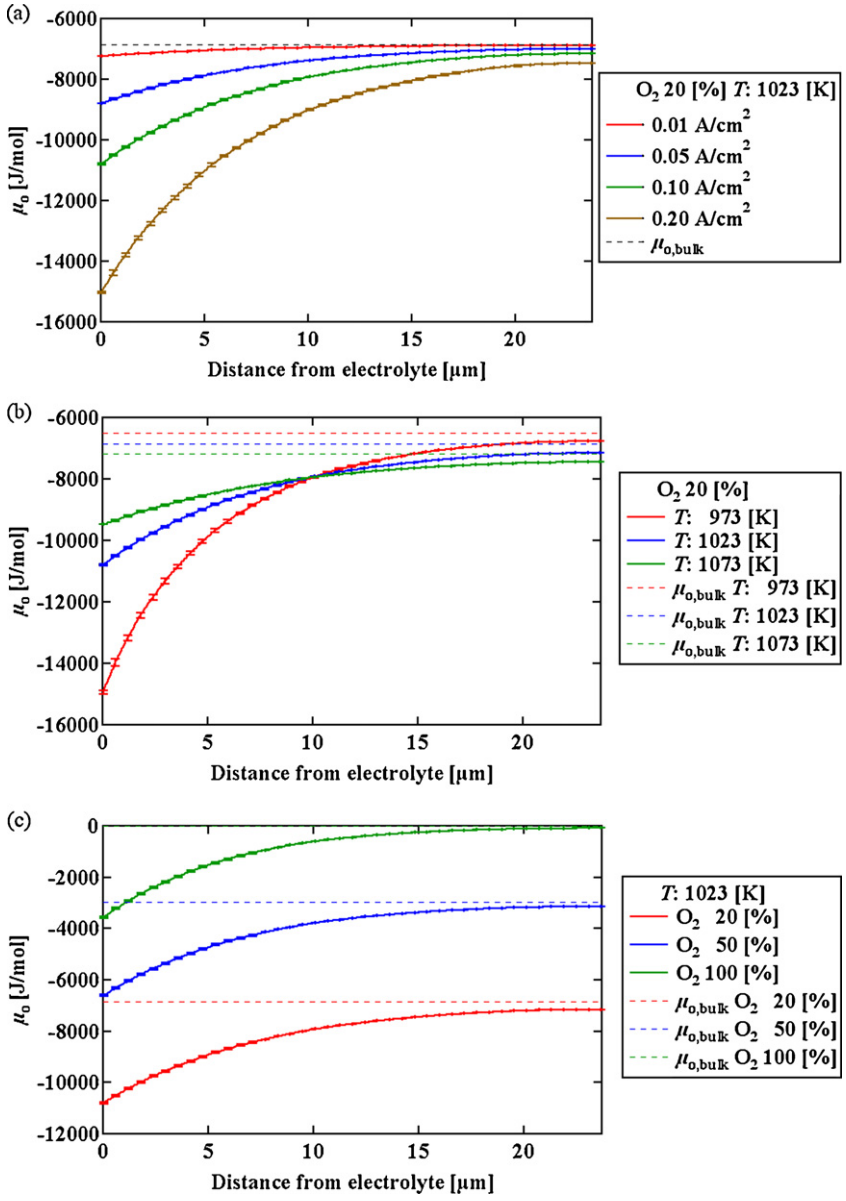

Fig. 12. Chemical potential distribution in LSCF cathode. (a) Dependences on current density at $O_2 = 20\%$ and $T = 1023$ K, (b) dependence on temperature at $O_2 = 20\%$ and $i = 0.1$ A/cm^2, and (c) dependence on O_2 concentration at $T = 1023$ K and $i = 0.1$ A/cm^2.

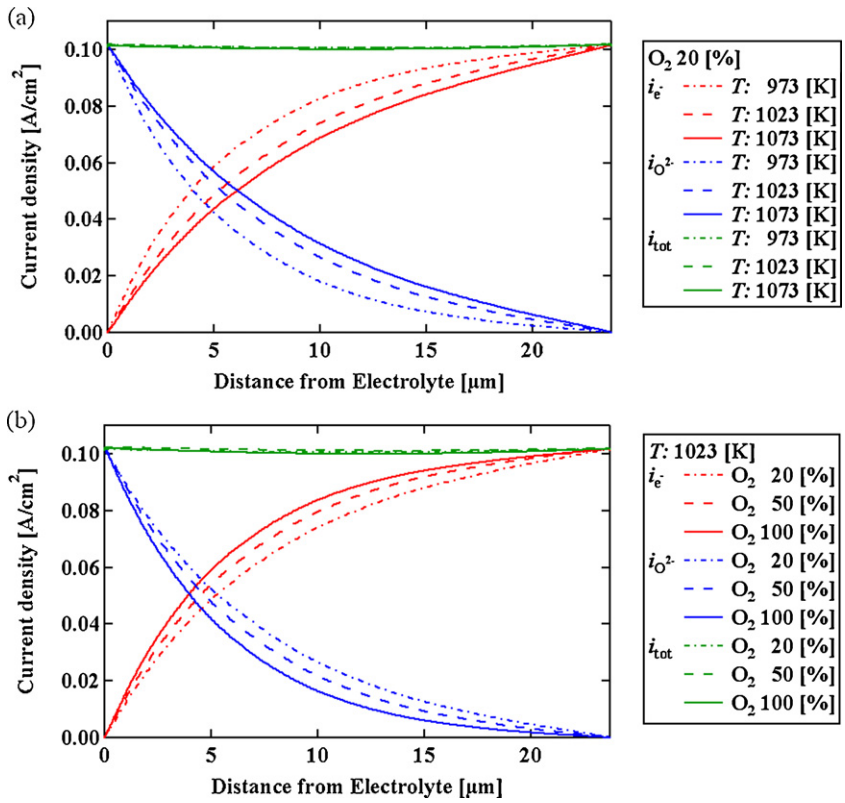

Fig. 13. Current density profiles along LSCF thickness direction. Dependences on (a) temperature, and (b) bulk O_2 concentration.

the LSCF phase. Electronic and ionic currents reach to the electrolyte and current collector sides, respectively. This indicates that the electrochemical reaction is taking place in the wide electrode region.

Fig. 12 shows averaged oxygen chemical potential μ_O profile along the LSCF thickness direction. Oxygen chemical potential decreases from the bulk value with the increase of current density as shown in Fig. 12(a). Chemical potential decreases mostly in the region within 15 μm from the electrolyte. The bars represent standard deviation (±1 sigma) of μ_O in the cross sectional plane. Thus, very uniform potential field is formed in the cross sectional plane. Fig. 12(b) shows oxygen chemical potentials at $i = 0.1$ A/cm^2. As shown in Fig. 12(b), oxygen chemical potential decreases near the electrolyte as temperature decreases. Since bulk μ_O is higher at lower temperatures due to the temperature dependence of μ_O as shown in Eq. (21), chemical potential profiles incidentally intersect at approximately 10 μm from the electrolyte. The slope of μ_O is steeper for 100% O_2 case than for the diluted cases at the vicinity of the electrolyte as shown in Fig. 12(c). This is because exchange current increases at higher p_{O_2} as shown in Eq. (27), while ionic conductivity remain nearly unchanged for this condition ($p_{O_2} > 0.075$ bar, $T = 1023$ K).

Due to the oxygen partial pressure dependence of diffusion coefficient shown in Fig. 6, decrease in oxygen chemical potential results in degradation of ionic conductivity near the electrolyte at low temperature and high current density conditions. This is considered to be the main reason for the diverged prediction at $O_2 = 20\%$, $T = 973$ K and $i = 0.2$ A/cm^2 case as discussed above. Further investigations on the p_{O_2} dependence of ionic conductivity, especially at low p_{O_2} and low temperatures, should be required for improving the accuracy of the numerical simulation especially for intermediate temperature SOFCs.

Fig. 13 shows ionic and electronic current distributions along LSCF thickness direction. As can be seen in Fig. 13(a), reactive region becomes thinner as temperature decreases. This is because of the degraded ionic conductivity at low temperature. On the other hand, reactive region gets thinner as bulk oxygen concentration is increased, as shown in Fig. 13(b). This is mainly due to the p_{O_2} dependence of exchange current as described in Eq. (27). Relative enhancement of surface reaction to ionic conduction at larger oxygen concentration reduces reactive region thickness.

5. Conclusions

Three-dimensional microstructure of $La_{0.6}Sr_{0.4}Co_{0.2}Fe_{0.8}O_{3-\delta}$ (LSCF6428) cathode is reconstructed by FIB-SEM, and its overpotential is predicted by the lattice Boltzmann method. Surface area estimated by the marching cube method showed fairly good agreement with those from stereology. Electron transfer to the adsorbed oxygen atom on the gas/solid interface is assumed to be the rate limiting step in the electrochemical modeling. The cathode overpotential prediction agreed well with the experimental data. However, predicted overpotential was very large at $O_2 = 20\%$, $T = 973$ K and $i = 0.2$ A/cm^2 case. This can be attributed to the decline in oxygen ionic conductivity at low p_{O_2}. Further investigation on oxygen partial pressure dependence of ionic conductivity is required for improving the accuracy of the numerical simulation. Three-dimensional chemical potential and current distributions are uniform and smooth, which indicates good ionic and electronic conductions as well as wide electrochemically active areas inside the LSCF microstructure. Present method will be an effective tool for investigating local oxygen potential field which affects local reactions, diffusions and physical properties of the MIEC cathodes.

Acknowledgments

This work was supported by the New Energy and Industrial Technology Development Organization (NEDO) under the Devel-

opment of System and Elemental Technology on Solid Oxide Fuel Cell (SOFC) Project.

References

[1] S.C. Singhal, K. Kendall, High Temperature Solid Oxide Fuel Cells, Elsevier, 2002.
[2] J. Mizusaki, Y. Mima, S. Yamauchi, K. Fueki, H. Tagawa, J. Solid State Chem. 80 (1989) 102–111.
[3] S.B. Adler, Chem. Rev. 104 (2004) 4701–4843.
[4] J.R. Wilson, W. Kobsiriphat, R. Mendoza, H.-Y. Chen, J.M. Hiller, D.J. Miller, K. Thornton, P.W. Voorhees, S.B. Adler, S. Barnett, Nat. Mater. 5 (2006) 541–544.
[5] D. Gostovic, J.R. Smith, D.P. Kundinger, K.S. Jones, E.D. Wachsman, Electrochem. Solid-State Lett. 10 (12) (2007) B214–B217.
[6] P.R. Shearing, J. Golbert, R.J. Chater, N.P. Brandon, Chem. Eng. Sci. 64 (2009) 3928–3933.
[7] H. Iwai, N. Shikazono, T. Matsui, H. Teshima, M. Kishimoto, R. Kishida, D. Hayashi, K. Matsuzaki, D. Kanno, M. Saito, H. Muroyama, K. Eguchi, N. Kasagi, H. Yoshida, J. Power Sources 195 (4) (2010) 955–961.
[8] J.R. Izzo Jr., A.S. Joshi, K.N. Grew, W.K.S. Chiu, A. Tkachuk, S.H. Wang, W. Yun, J. Electrochem. Soc. 155 (5) (2008) B504–B508.
[9] P.R. Shearing, J. Gelb, J. Yi, W.-K. Lee, M. Drakopolous, N.P. Brandon, Electrochem. Commun. 12 (8) (2010) 1021–1024.
[10] A.S. Joshi, K.N. Grew, A.A. Peracchio, W.K.S. Chiu, J. Power Sources 164 (2007) 631–638.
[11] P. Asinari, M.C. Quaglia, M.R. von Spakovsky, B.V. Kasula, J. Power Sources 170 (2007) 359–375.
[12] Y. Suzue, N. Shikazono, N. Kasagi, J. Power Sources 184 (2008) 52–59.
[13] N. Shikazono, D. Kanno, K. Matsuzaki, H. Teshima, S. Sumino, N. Kasagi, J. Electrochem. Soc. 157 (5) (2010) B665–B672.
[14] P.R. Shearing, J. Gelb, J. Yi, W.-K. Lee, M. Drakopolous, N.P. Brandon, J. Power Sources 195 (15) (2010) 4804–4810.
[15] J. Fleig, Phys. Chem. Chem. Phys. 7 (2005) 2027–2037.
[16] W.E. Lorensen, H.E. Cline, Comput. Graphics 21 (1987) 163–169.
[17] J. Lindblad, I. Nyström, Lect. Note Comput. Sci. 2301 (2002) 61–71.
[18] R.T. DeHoff, F.N. Rhines, Quantitative Microscopy, McGraw-Hill, 1968.
[19] R. Krishna, J.A. Wesselingh, Chem. Eng. Sci. 52 (1997) 861–911.
[20] V. Novák, P. Štěpánek, P. Kočí, M. Marek, M. Kubíček, Chem. Eng. Sci. 65 (7) (2010) 2352–2360.
[21] H.J. Bouwmeester, M.W. Otter, B.A. Boukamp, J. Solid State Electrochem. 8 (2004) 599–605.
[22] J. Fleig, F.S. Baumann, J. Maier, ECS Proceedings, 2005–2007, 2005, pp. 1636–1644.
[23] A. Esquirol, N.P. Brandon, J.A. Kilner, M. Mogensen, J. Electrochem. Soc. 151 (2004) A1847–A1855.
[24] T.H. Zeiser, P. Lammers, E. Klemm, Y.W. Li, J. Bernsdorf, G. Brenner, Chem. Eng. Sci. 56 (2001) 1697.